ENSTA Bretagne
Ifremer
15ÈMES JOURNÉES DE L'HYDRODYNAMIQUE
22 - 24 novembre 2016 - Brest

COMPARAISON D'UNE MÉTHODE DE LIGNE PORTANTE 3D NON LINÉAIRE AVEC DES SIMULATIONS RANSE 3D ET APPLICATION A LA PRÉDICTION DU CHARGEMENT GLOBAL D'UN CERF-VOLANT EN VIRAGE

COMPARISON OF 3D NON-LINEAR LIFTING LINE METHOD CALCULATIONS WITH 3D RANSE SIMULATIONS AND APPLICATION TO THE PREDICTION OF THE GLOBAL LOADING ON A CORNERING KITE

C. Duport[1] *, J.-B. Leroux[1], K. Roncin[1], C. Jochum[1], Y. Parlier[2]

[1]ENSTA Bretagne, IRDL, CNRS FRE 3744, 2 Rue François Verny, 29806 Brest cedex 9, France
[2]Beyond the sea, 1010 Avenue de l'Europe, 33260 La Teste de Buch, France
*chloe.duport@ensta-bretagne.org

Résumé

Dans le cadre de la conception et de l'exploitation de cerfs-volants pour la propulsion auxiliaire de navires, il est nécessaire d'être capable de prévoir rapidement la traction que peut fournir un kite en fonction de sa trajectoire. Dans un premier temps, un modèle 3D non linéaire basé sur la ligne portante de Prandtl a été mis au point à cet effet. Il permet le calcul rapide des efforts aérodynamiques d'une aile avec des angles de dièdre, de vrillage et de flèche, variables en envergure ; pour des cinématiques de vol prenant en compte vitesses de translation et taux de rotation. Ce modèle a été vérifié grâce à des simulations RANSE 3D et donne des résultats satisfaisants en incidence et en dérapage, avec par exemple des écarts d'environ 5% pour les prévisions en portance. Une attention particulière a été apportée à l'estimation de la précision des résultats numériques produits. Dans un second temps, ce modèle a été introduit dans une nouvelle procédure itérative d'équilibrage du kite, qui a été utilisée pour estimer son chargement en vol dynamique sur une trajectoire circulaire. Dans ce cas, l'influence des taux de rotation sur le chargement est mise en évidence. Une étude paramétrique a finalement été menée pour évaluer et analyser les variations des coefficients aérodynamiques caractéristiques du vol en fonction de la longueur des lignes et du rayon de la trajectoire.

Summary

As part of the design and operation of kites as auxiliary propulsion of vessels, it is necessary to be able to quickly estimate the traction that can provide a kite according to its trajectory. At first, a 3D non-linear model based on the lifting line of Prandtl has been developed for this purpose. It allows the rapid calculation of aerodynamic forces for a wing with any laws for the dihedral angle, the twist, and the sweep angle, along the span; and for a general flight kinematic taking into account translation velocities and rotation rates. This model has been verified by comparison with 3D RANSE simulations and produces satisfactory results in incidence and sideslip, with such gaps of about 5% for forecasts lift. Special attention has been given to the estimation of the accuracy of the provided numerical results. Secondly, this model has been introduced in a new equilibrium iterative procedure for the kite, which has been used to estimate the loading of a dynamic kite flying on a circular path. In this case the influence of the rotation rates on the loading is highlighted. A parametric study has finally been conducted to assess and analyse the changes in aerodynamic coefficients flight characteristics depending on the tether length and the radius of the trajectory.

1 Introduction

This work is part of the beyond the sea® project which aims to develop tethered kite systems for auxiliary propulsion of merchant ships. It is necessary to develop an aerodynamic model in order to estimate the kite properties. Knowing the computational time needed to carry out the CFD simulation of a kite, it can be very useful in a design stage to use a fast, reliable and simple model to estimate rapidly the kite aerodynamic performances. As the kite can follow a complex trajectory, the method has also to take into account any sideslip angle or turn rate of the kite.

The zero-mass model is often used to estimate the kite performances. In this model, the weights of the kite and of the tethers are neglected and the lift-to-drag ratio of the kite wing is a fundamental given. Dadd [4] used it in order to predict the kite velocity and the tether forces. However Dadd assumed that the kite lift and drag coefficients remain constant during the flight. Furthermore the aerodynamic coefficients were measured experimentally and then estimated for different angles of incidence with formulas from the Prandtl lifting line theory. It is certainly hard to consider experimental measurements each time a new kite geometry is tested. Gaunaa [5] developed a computationally efficient method to determine the aerodynamic performances of kites. The approach iteratively couples a Vortex Lattice Method (VLM) with 2D airfoil data to consider the effects of airfoil thickness and of viscosity. The results were compared with RANSE simulations and showed good agreement for cases without stall. Nevertheless only kite in symmetrical translation motions were considered in this work.

The Prandtl lifting line method is also used for wings performances prediction. As an example Graf [6] used a non-linear iterative lifting line method to predict the lift and drag of a two-element straight wing for an AC72 catamaran. The comparison with RANSE simulations showed as well a good agreement for attached flow regime. Leloup [10] adapted the lifting line method for 3D kite wings with variable dihedral and sweep angles along the span. However in this work a direct solving, based on a collocation method, was used and prohibits to take into account the non-linearity of the lift coefficient.

This study first presents in section 2 the geometry of the kite and its parametric definition. The section 3 details the 3D non-linear lifting line method which was implemented to cope with wings with high dihedral and sweep angles. In section 4, the different RANSE simulations, which have been carried out in order to validate the 3D non-linear lifting line results, are described, and then the comparative results are discussed. Eventually section *5* presents a use of the method to simulate the flight of a kite on a circular trajectory.

2 Parametric definition of the kite geometry

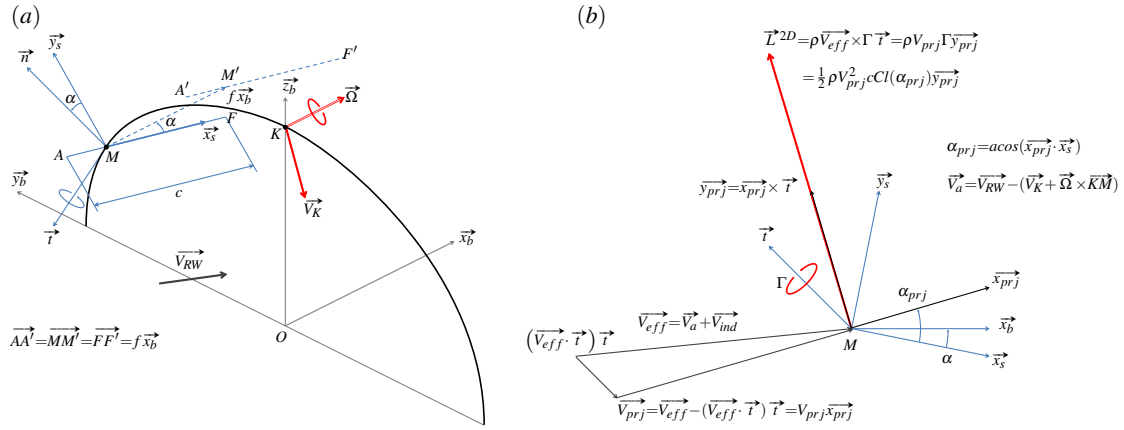

Figure 1 – (a) Definition of the kite geometry. (b) Local effective wind and local lift per unit length in the section plane.

The kite geometry is defined in the Cartesian reference frame $(O,\vec{x_b},\vec{y_b},\vec{z_b})$ (see Figure 1 (a)). A generatrix line is given as a parametric planar curve $M(s)$ in the plane $(O,\vec{y_b},\vec{z_b})$, M denoting the current point and s the curvilinear abscissa. In general this line is chosen symmetrical with respect to the axis $(O,\vec{z_b})$. At the current point $M(s)$, the section of the kite is defined in the normal plane with respect to the tangent vector to the generatrix line $\vec{t}(s)=\overrightarrow{dM}/ds$. This plane is denoted $(M(s),\vec{x_b},\vec{n}(s))$, where $\vec{n}(s)=\vec{x_b}\times\vec{t}(s)$ is the normal vector in the $(O,\vec{y_b},\vec{z_b})$ plane to the generatrix line. The local chord direction $\vec{x_s}(s)$ is obtained from the rotation of an angle $\alpha(s)$ around $\vec{t}(s)$ of the vector $\vec{x_b}$, where $\alpha(s)$ is a given twist law. $M(s)$ is supposed to be the quarter chord point of the current section. The leading edge $A(s)$ and the trailing edge $F(s)$ are then placed along the chord axis $(M(s),\vec{x_s}(s))$ according to a given chord law $c(s)$, following $\overrightarrow{AM}(s)=0.25c(s)\vec{x_s}(s)$ and $\overrightarrow{MF}(s)=0.75c(s)\vec{x_s}(s)$. This finally leads to the local chord reference frame of the kite section $(A(s),\vec{x_s}(s),\vec{y_s}(s))$ with $\vec{y_s}(s)=\vec{x_s}(s)\times\vec{t}(s)$, where the points of the extrados and intrados can be placed; for example from a given non dimensional

section definition, scaled with the chord law $c(s)$. In the case of a kite wing with sweep angle, the local section points are finally translated by the vector $f(s)\vec{x_b}$, with $f(s)$ a given sweep law.

Within this study, the chosen kite geometry is un-twisted and un-swept, and is constructed as previously described, with a semi-circular generatrix line and a linear chord law varying from the root section in the symmetry plane to the tip section. The kite section is kept constant along the span, and is defined by the NACA2412 points. For the numerical verification results presented section 4, the radius of the generatrix line is $1.5m$, and the chords are $1.0m$ at root and $0.5m$ at tips. For the simulations of kite's circular flights in section 5, the radius of the generatrix line is $3.0m$, and the chordlaw is constant of $2.0m$.

3 3D non-linear lifting line method

The 3D non-linear lifting line is based on an extension of the Prandtl's lifting line theory. This extension is intended to address cases of wings with variable dihedral and sweep angles. Leloup introduced in [10] a linear implementation while the present method is taking into account the non-linearity of the lift coefficient. The kite wing is supposed to fly in a given wind $\overrightarrow{V_{RW}}$, with a given velocity $\overrightarrow{V_K}$ at the quarter chord point K in its symmetry plane, and with a given turn rate $\vec{\Omega}$. In this general case, the kite global apparent wind is $\vec{V_a} = \overrightarrow{V_{RW}} - \overrightarrow{V_K}$ whose direction is denoted $\vec{x_a}$. The finite wing and its wake are represented by a set of horseshoe vortices of different strengths $\Gamma = (\Gamma_i)_{i=1...n}$. The aim of the algorithm presented thereafter is to calculate the circulation Γ_i of each horseshoe vortex. Once these strengths are obtained, the local effective flow for each wing section allows local aerodynamic forces and torques calculation along the span of the wing. The numerical iterative solution is taken from Anderson [2], but the calculation of the local effective angles of incidence is adapted to the cases of wings which are non-straight and non-planar. The horseshoe vortices used for discretisation, and calculation of their influences, are for their part derived from Katz and Plotkin [8].

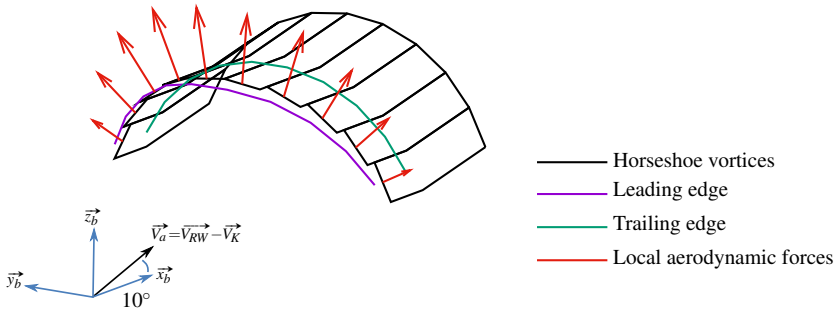

Figure 2 – Example of a low discretised lifting line model, of a kite in translation at 10° of incidence. Red vectors are proportional to the local aerodynamic resulting forces. Local torques are not represented to improve readability.

The wing is divided in a finite number n of plane sections parallel to $\vec{x_b}$, as defined in section 2, each one represented by a horseshoe vortex. The horseshoe vortex number i consists of six vortex segments. The bound vortex $\Gamma_i \vec{t_i} ds_i$ is located at the local quarter chord length, perpendicular to the plane of the considered section. Each of the two trailing vortices are separated into two parts: the first which extends parallel to the chord over one chord length, $\pm\Gamma_i \overrightarrow{x_s}_i c_i$, and the second which extends parallel to the global relative free stream direction $\vec{x_a}$ and over several chords length leading to l_i length, $\pm\Gamma_i \vec{x_a} l_i$. The starting vortex $-\Gamma_i \vec{t_i} ds_i$ is finally used to close the horseshoe vortex. An example of the discretised model is presented in Figure 2. Note that even with a swept wing, the bound vortex along the lifting line is orthogonal to the two adjacent trailing vortices. This leads to a piecewise constant discretisation of the lifting line, but it is necessary in order to have a correct match between the local lift calculated from the Kutta formula or from the polar of the section (see Figure 1 (b)), as theoretically required in such models. For the section i of the kite, the local apparent wind is given by $\overrightarrow{V_a}_i = \overrightarrow{V_{RW}} - (\overrightarrow{V_K} + \vec{\Omega} \times \overrightarrow{KM_i})$. 2D polar curves for the coefficients of lift (Cl_i), drag (Cd_i), and moment about the quarter chord point (Cm_i), are also supposed to be given with respect to the angle of incidence.

The numerical iterative solution for the circulation Γ_i of each horseshoe vortex is described hereafter with p the counter of the recursive steps. The local circulation values are first initialized by an elliptical or other distribution along the wing span, denoted $\Gamma_i^{(0)}$ for $p = 0$. At step p, starting from the $\Gamma_i^{(p)}$ values, the $\Gamma_i^{(p+1)}$ values are updated as follow. For each point M_i of the lifting line, the induced velocities by each vortex segment are calculated from $\Gamma_i^{(p)}$ values with the Biot-Savart law and then summed, leading to the induced velocity $\overrightarrow{V_{ind\ i}}^{(p)}$. Combined with the local free stream velocity $\overrightarrow{V_a}_i$, one obtains the effective wind $\overrightarrow{V_{eff\ i}}^{(p)}$. This velocity is projected in the plane of the section, leading to $\overrightarrow{V_{prj\ i}}^{(p)} = \overrightarrow{V_{eff\ i}}^{(p)} - (\overrightarrow{V_{eff\ i}}^{(p)} \cdot \vec{t_i})\vec{t_i}$ and to the section angle of effective incidence $\alpha_{prj\ i}^{(p)}$. Using the 2D lift polar curve

of the section, one obtains the local lift per unit length, in the section plane, orthogonal to $\overrightarrow{V_{prj\ i}}^{(p)}$, and of modulus $L_i^{(p)} = 0.5\rho V_{prj\ i}^{(p)2} c_i Cl_i(\alpha_{prj\ i}^{(p)})$ (see Figure 1 (b)). By construction this local lift is orthogonal to the $(\overrightarrow{V_{eff\ i}}^{(p)}, \vec{t_i})$ plane, as it should be according to the Kutta formula $\vec{L_i}^{(p)} = \rho \overrightarrow{V_{eff\ i}}^{(p)} \times \Gamma_i \vec{t_i}$ applied to the bound vortex. The value of the bound vortex strength $\Gamma_i^{(p+1)}$ is finally settled so that the Kutta formula also leads to the previous modulus $L_i^{(p)}$. In other words, $\Gamma_i^{(p+1)}$ is calculated solving $\|\rho \overrightarrow{V_{eff\ i}}^{(p)} \times \Gamma_i \vec{t_i}\| = L_i^{(p)}$ for the unknown Γ_i, which naturally leads to $\Gamma_i^{(p+1)} = 0.5 * V_{prj\ i}^{(p)} c_i Cl_i(\alpha_{prj\ i}^{(p)})$. The circulation value is ultimately updated by weighting between current $\Gamma_i^{(p+1)}$ and previous $\Gamma_i^{(p)}$ values using a damping factor. This whole process is repeated and, as expected, the circulation distribution is found to converge according to a stopping criteria of the form $\|\Gamma^{(p+1)} - \Gamma^{(p)}\| < (10\|\Gamma^{(p+1)}\| + 1) * 10^{-N}$.

Once convergence is reached, the lift, drag and torque of each section of the wing are then post processed with the converged circulation, which leads to integrated local loads. Finally, these are vectorially summed, to obtain the global force and the global moment about the K point, which apply to the kite wing.

The converged result is found to be independent of the initial solution. Mesh convergence studies were performed. In the cases of straight wings in translation motion parallel to their symmetry plane, very good results versus analytical ones were obtained with at least 10 horseshoe vortices. Nevertheless, in the cases of 3D wings with variable dihedral and sweep, a larger mesh dependency of the converged results was observed, in particular for the total drag coefficient. In the following, the lifting line results are presented for a wing discretised with 40 sections. The mesh having been varied from 10 to 200 sections, the confidence intervals at 95% were estimated using the standard deviations of the results. In the linear range, for angles of incidence typically lower than 10°, it was obtained: 1.0% for the lift, 1.3% for the drag and 1.6% for the moment about the K point. In the non-linear range, for angles of incidence typically greater than 10°, it was obtained: 4.0% for the lift, 15.3% for the drag and 14.1% for the moment about the K point.

4 Verification of the 3D lifting line method with StarCCM+® simulations

In order to validate the 3D non-linear lifting line method, its results were compared to those obtained from 3D RANSE simulations. The 2D and 3D RANSE necessary simulations were performed with the generalist tool STAR-CCM+®. The 2D simulations were used for convergence studies, but also to obtain the 2D polar curves of the kite section, which were required to feed the 3D non-linear lifting line model. In a second step, the 3D simulations were used to calculate the global aerodynamic efforts of a kite in translation, with respect to variations of the angle of incidence and the sideslip angle.

4.1 General numerical set up

Within this study, all the RANSE simulations were incompressible, steady and fully turbulent. The retained turbulence model was the two-equation k-ε realizable model with a two-layer formulation for the wall treatment. The segregated flow solver was based on the SIMPLE algorithm, and a second-order discretisation scheme. It was chosen to work with a kite section or a kite wing fixed with respect to the computational domain, and to vary the direction of the inlet velocity in order to model the angle of incidence and the sideslip angle. The inlet boundary conditions were such that the chord based Reynolds number was $3.1 * 10^6$, for the root section of the kite. The turbulence intensity was set to 0.5% and the turbulent viscosity ratio was set to 1.

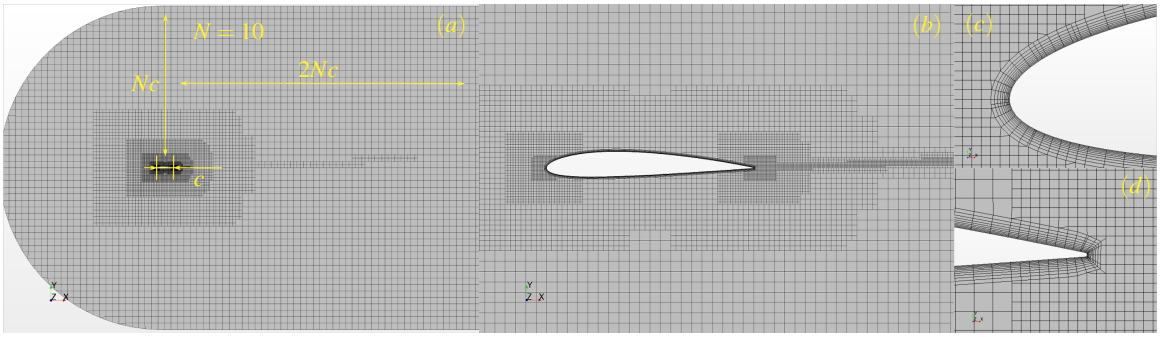

Figure 3 – (a) 2D meshed computational domain. (b) View of the mesh around the profile section. View of the near wall mesh in the vicinity of (c) the leading edge and (d) the trailing edge.

The meshed computational domain is presented Figure 3 (a) for the 2D simulations and Figure 4 (a) for the 3D simulations. The domain was meshed using the trimmed cell mesher, which led to predominantly hexahedral mesh (Figure 3 (a)). It was controlled by a cell base size $(0.1c)$, and targeted cell sizes at some boundaries: inlet and outlet

(0.5c), wing extrados and intrados (0.025c), wing leading and trailing edges (0.00625c). The cells size growth rate was very slow, which means at least 8 equal sized cell layer per transition (Figure 3 (b)). Around the wing a prism layer mesh was used in order to get orthogonal cells next to the wall (Figure 3 (c) and (d)). It was controlled by its thickness (0.0125c), a number of layers (10), and a growth rate between adjacent cells in the wall normal direction (1.2). In 2D two anisotropic wake refinements were also prescribed in the mean free stream direction from the trailing edge, one finely meshed of one chord long and the other coarse, extending over several chord (15c) (Figure 3 (a) and (b)).

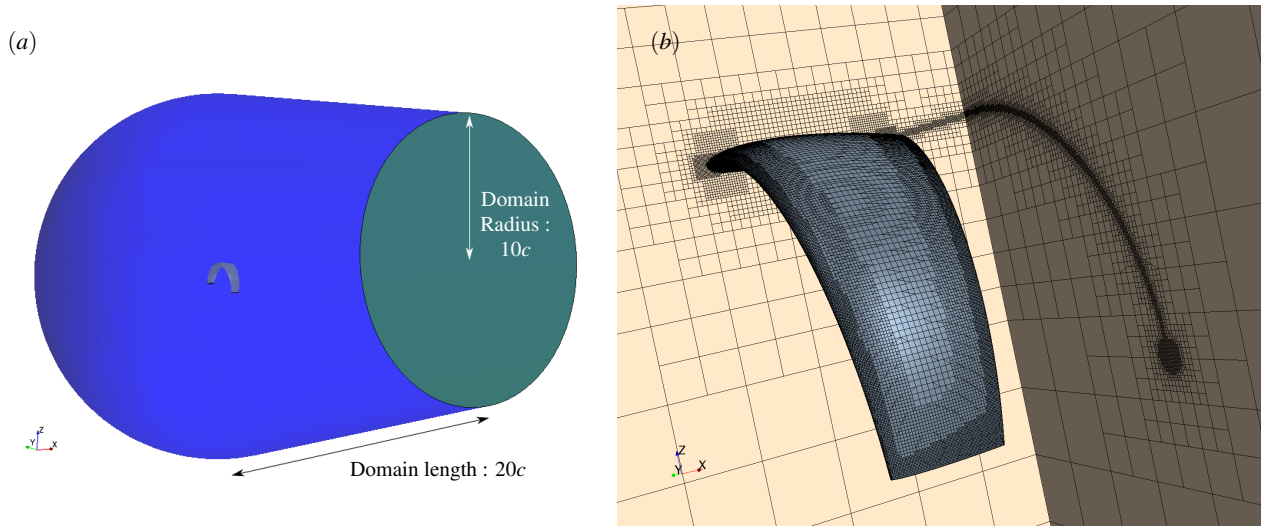

Figure 4 – (a) 3D computational domain. (b) 3D mesh sections which illustrate the refinements in the wake and around the tip vortex.

In 3D the wake refinements were prescribed on the cylinder which is supported on the trailing edge and whose axis is parallel to the mean free stream, over the same extent as in 2D. In order to partially resolve the tip vortex, a supplementary refinement was also prescribed in a conical region, which includes the wing tip and whose axis is parallel to the mean free stream. These refinements are illustrated Figure 4 (b). The obtained 2D and 3D meshes were coarse, of about $16*10^3$ cells in 2D and $4.7*10^6$ cells in 3D, and they led to a mean value of $y+$ over the wing surface of about 35 in each simulated cases. The stopping criteria of the simulations were based on the monitor of the lift and drag coefficients, specifying a $|max-min|$ tolerance over the 10 last calculated values. The tolerance was set to 10^{-6} for both coefficients, and it was found that it corresponded to the fall of the non-dimensional residuals over at least 4 or 5 decades.

4.2 Estimation of the numerical accuracy of the RANSE simulations

An attempt was done to estimate a numerical accuracy of the 2D and 3D RANSE results. It was supposed that results from 2D simulations were sufficient for that purpose and that they could be extrapolated to 3D cases. In addition, it was assumed sufficient to examine a single angle of incidence of 2 ° for the root kite section, to be representative.

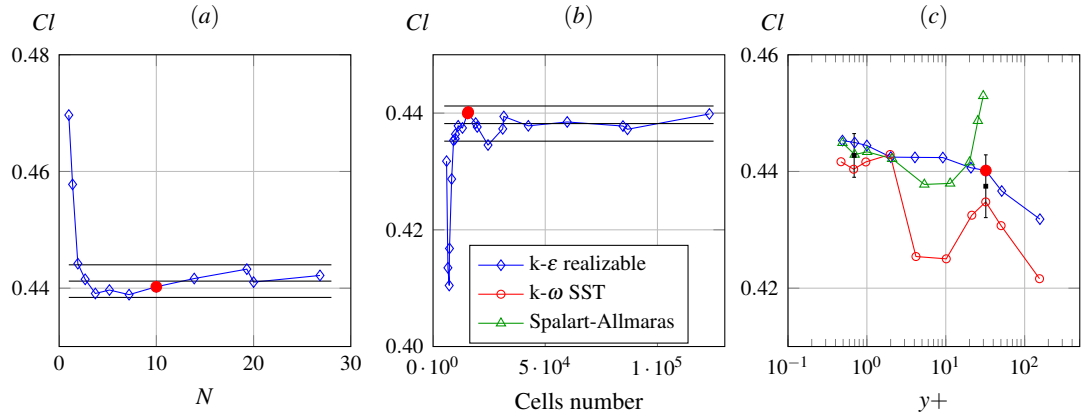

Figure 5 – Convergence history of the lift coefficient for variations (a) of the computational domain size, (b) of the number of cells in the mesh, (c) of the number of layers of the near wall mesh and of the turbulence model.

Three elementary variations of the general numerical set up of section 4.1 were considered. The results in term of lift coefficient are presented Figure 5. The obtained curves are similar for the coefficients of drag or moment. First (Figure 5

(a)), the size of the computational domain was varied (parameter N from 1 to 27, see Figure 3 (a)), keeping constant the base size, the absolute targeted sizes at the section, the near wall mesh parameters, and the growth rate. Second (Figure 5 (b)), the targeted sizes at each boundary being defined relatively to base size, the base size was varied (from $0.6c$ to $0.02c$, leading to a number of cells from $6*10^3$ to $120*10^3$), keeping constant the near wall mesh parameters. Third (Figure 5 (c), the number of layers of the near wall mesh was varied (from 4 to 32, leading to mean $y+$ values from 156 to 0.5), keeping constant all the other mesh parameters. In this last case, two other turbulence model were also tested (k-ω SST and Spalart-Allmaras).

For the variations of the domain size and of the number of cells (Figure 5 (a) and (b)), based on the limited number of computed points, for each aerodynamic coefficient, it was estimated a mean converged value (denoted cvg), a standard deviation relative to this mean (denoted rms), and then a 95% confidence interval. For the variations of the near wall mesh and of the models (Figure 5 (c)), respectively around $y+ \sim 1$ and $y+ \sim 30$, it was estimated first the coefficients mean values (also denoted cvg) and their standard deviations relative to these means due to model variations (also denoted rms), and second the relative difference between coarse and fine mesh mean results (denoted dif). These are plotted in black Figure 5, and it was found that in each case the confidence interval enclose the red filled point corresponding to the general numerical set up of section 4.1. It can also be noticed Figure 5 (c), as expected, that intermediate meshes in the buffer layer, for $y+$ in the range of $[5;30]$, led to highly model dependent results, and that the Spalart-Allmaras model is valid only for fine meshes around $y+ = 1$.

			Figure 5(c)		
	Figure 5 (a) $2Crms/Ccvg$	Figure 5 (b) $2Crms/Ccvg$	$y+ \sim 1$ $2Crms/Ccvg$	$y+ \sim 30$ $2Crms/Ccvg$	$Cdif$
Lift	0.6%	0.7%	0.8%	1.2%	1.2%
Drag	1.7%	2.5%	5.0%	1.5%	2.0%
Moment	0.9%	1.5%	1.5%	2.4%	2.3%

Table 1 – Estimation of the deviations, coming from the variations of the domain size, of the mesh and of the turbulence model. C stands for coefficient.

More precisely, the estimated deviation results for the coefficients of lift, of drag and of moment, are resumed in the Table 1. From this table it was finally estimated that the numerical results provided by the coarse meshed numerical set up of section 4.1 were unconfined, mesh converged, and model independent, with the following relative accuracies: $\pm 3.7\%$ for the lift, $\pm 7.7\%$ for the drag and $\pm 7.1\%$ for the moment.

4.3 Numerical results

2D RANSE simulations were carried out on the NACA2412 section for 14 angles of incidence within the range of $[-8°;16°]$. The numerical results were compared with experimental ones obtained in wind tunnel [1] at the same Reynolds number. The parametric polar curves used for the lifting line method were established by approaching the RANSE results at best. All these results are presented Figure 6. The agreement between experimental and numerical results is excellent for the lift coefficient and satisfactory for the coefficients of drag and of moment. For the last two, one of the explanation for the differences is that simulations are fully turbulent whereas the experiments were performed on a smooth section in a low residual turbulence wind tunnel.

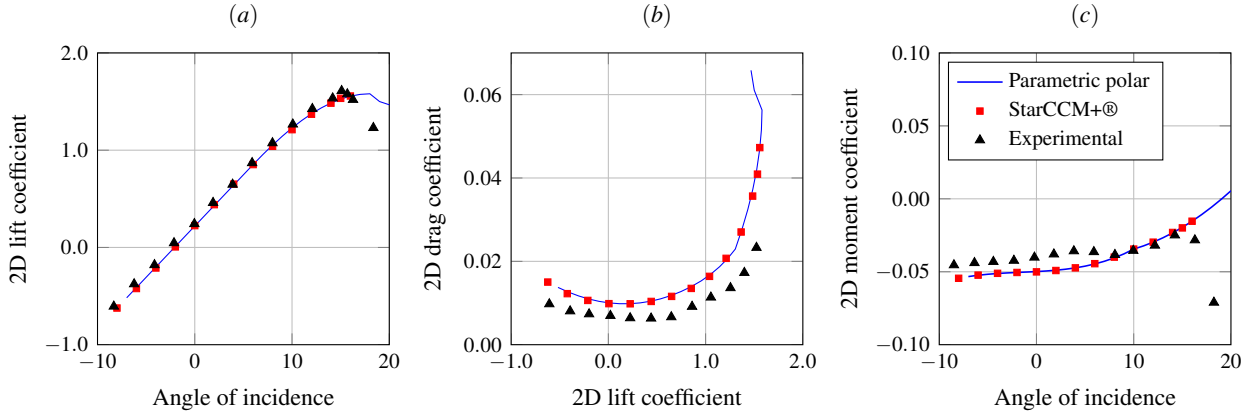

Figure 6 – 2D polar curves obtained via StarCCM+® (filled squares), compared with experimental data [1] (filled triangles), and fitted with parametric polar curves used in the lifting line method (plain line).

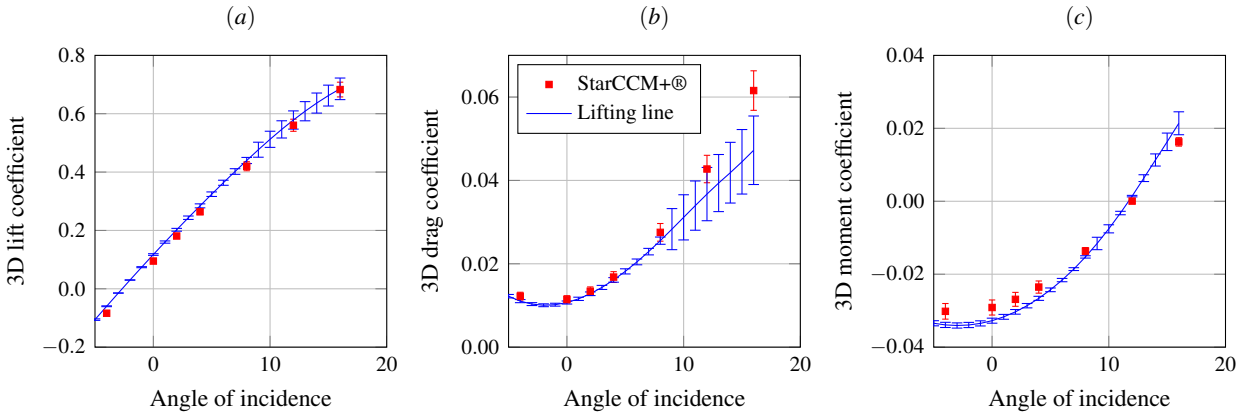

Figure 7 – 3D aerodynamic coefficients with respect to the angle of incidence, obtained via StarCCM+® (filled squares) and the lifting line method (plain line) on a 3D kite. Error bars are the estimated numerical accuracies.

For the validation of the lifting line method, 3D RANSE simulations have been carried out. Figure 7 shows the three aerodynamic coefficients for a kite purely in incidence. The error bars are the confidence interval at 95% for the StarCCM+® results and for the mesh dependency of the lifting line method as presented section 3 and section 4.2. The difference between the RANSE results and the lifting line method are around 5% for the lift coefficient. For the drag coefficient, there is a 5% gap at low angle of incidence up to 20% for the higher angles of incidence. The difference between the two approaches for the moment coefficient is of 12% in average.

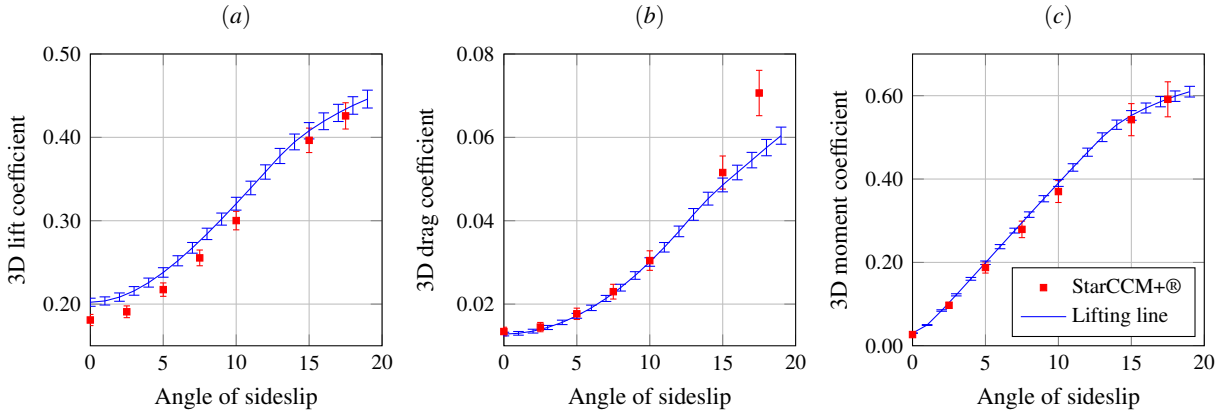

Figure 8 – 3D aerodynamic coefficients with respect to the sideslip angle obtained via StarCCM+® (filled squares) and the lifting line method (plain line) on a 3D kite at 2° of incidence. Error bars are the estimated numerical accuracies.

Simulations were also carried out for the kite at 2° of incidence with different sideslip angles (see Figure 8). The lift coefficient is estimated from the aerodynamic resultant orthogonal to the wind direction. For the three aerodynamic coefficients, roughly the same gap is found between the kite purely in translation at 2°of incidence and the kite at 2°of incidence with any sideslip angle included in $[0°;15°]$. The difference is approximately of 10% for the lift coefficient between the RANSE simulation and the lifting line method. For the drag and moment coefficients, it is only of a few percent. At 15° of sideslip angle, the results start to differ more significantly for the drag coefficient. Following the results presented Figure 7 and Figure 8, and taking into account the computation time of each approaches, the lifting line results are quite satisfying for a large range of incidence and a sideslip angle included between 0° and 15°.

5 Rigid kite with a circular path

A kite develops its maximum power in a dynamic flight thanks to its own velocity. Dadd *et al.* [4] used the zero-mass model to predict the kite forces on an eight shaped trajectory. Within this model, the kite is reduced to the point K, and the tethers are reduced to only one rectilinear equivalent, whose direction and constant length are $\vec{z_{k0}}$ and L_T, such that $\overrightarrow{OK} = -L_T\vec{z_{k0}}$, O being the anchor point. The weights of the kite and of the tethers are neglected. The kite is assumed to be in pure translation against the apparent wind $\vec{V_a} = \overrightarrow{V_{RW}} - \vec{V_K}$, supposed to be parallel to the kite symmetry plane $(K, \vec{x_b}, \vec{z_b})$. Under such assumptions, being given the wind $\overrightarrow{V_{RW}} = V_{RW}\overrightarrow{x_{RW}}$, the spherical coordinates of the kite, the flight direction $\overrightarrow{x_{V_K}}$,

and a lift-to-drag ratio ε, it is possible to derive analytically the modulus of the kite velocity V_K and the apparent wind $\vec{V_a}$ [9] (and finally the resulting force, a global lift coefficient being also given). In order to avoid to postulate ε, the global angle of incidence of the kite α_g relative to the tangent plane in K at the flight sphere being assumed to be known, Leloup [9] proposed an iterative procedure to calculate the effective value of the lift-to-drag ratio at each point of a prescribed trajectory. Nevertheless, the kite is always assumed to be in pure translation against $\vec{V_a}$, and its turn rate is neglected, while it certainly induces an asymmetrical loading and may change significantly the equilibrium.

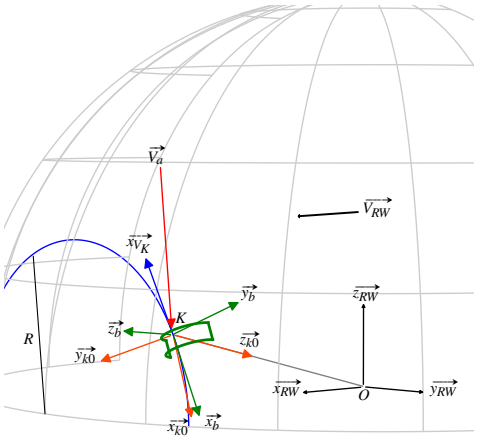

Figure 9 – Circular path of the kite as discussed in section 5, with with $\vec{V_{RW}}$ the wind, $\vec{x_{V_K}}$the kite velocity direction, $\vec{V_a}$ the apparent wind seen by the kite, O the anchor point and R the radius of the trajectory.

In this section, a new procedure is proposed to calculate the effective lift-to-drag ratio of a kite along a prescribed flight path, taking into account the turn rate influence. In a first step, the investigated trajectory is a circular trajectory of axis $(O,\vec{x_{RW}})$ around the full power point, $\vec{x_{RW}}$ being the wind direction (see Figure 9). Due to symmetry, the flight of the kite is steady in this case, and the turn rate $\vec{\Omega}$ can easily be calculated.

5.1 Equilibrium iterative procedure for the kite

The wind $\vec{V_{RW}}$, the length L_T of the equivalent tether, the radius R of the trajectory of the point K, and the kite geometry being prescribed, the goal is to find the equilibrium position of the kite, still assuming zero mass and the relative wind $\vec{V_a} = V_a\vec{x_a}$ parallel to the symmetry plane $(K,\vec{x_b},\vec{z_b})$. The vector $\vec{x_{k0}}$ is defined as the direction vector of the projection of $\vec{x_a}$ or $\vec{x_b}$ on the tangent plane in K at the flight sphere. The basis of the tangent plane is completed with $\vec{y_{k0}} = \vec{z_{k0}} \times \vec{x_{k0}}$. Three pseudo-degrees of freedom are introduced to position the kite relatively to the tangent plane in K at the flight sphere: a geometrical angle of incidence α_g around $(K,\vec{y_{k0}})$ from $\vec{x_b}$ to $\vec{x_{k0}}$, a roll angle γ around $(K,\vec{x_{k0}})$ from $-\vec{y_{k0}}$ to $\vec{y_b}$, and a yaw angle β around the tether axis $(K,\vec{z_{k0}})$ from $\vec{x_{k0}}$ to $-\vec{x_{V_K}}$. α_g is a given, is kept fix, and is supposed to result from an adjustment of the real front/back tethers. γ and β are unknown variables. γ is supposed to result from an adjustment of the real left/right tethers, while β is supposed to result from a self-positioning of the kite.

Since this flight case is steady, no matter the chosen point K along the studied circular trajectory, the flight direction $\vec{x_{V_K}}$ is known, and the iterative algorithm starts with an estimated lift-to-drag ratio $\varepsilon^{(0)}$ and a roll angle $\gamma^{(0)} = 0$. Denoting the counter of the recursive steps p, the kite velocity $V_K^{(p)}$ can be calculated via the zero-mass model formula with Equation 1 [9], then the apparent wind by $V_a^{(p)}\vec{x_a}^{(p)} = V_{RW}\vec{x_{RW}} - V_K^{(p)}\vec{x_{V_K}}$. The rotation rate of the kite is also calculated with Equation 2.

$$V_K^{(p)} = V_{RW}\left[(\vec{x_{RW}}\cdot\vec{x_{V_K}}) + \sqrt{(\vec{x_{RW}}\cdot\vec{x_{V_K}})^2 + \left(\frac{\vec{x_{RW}}\cdot\vec{z_{k0}}}{\sin(\varepsilon^{(p)})}\right)^2 - 1}\right] \tag{1}$$

$$\vec{\Omega}^{(p)} = \frac{V_K^{(p)}}{R}\vec{x_{RW}} \tag{2}$$

By projection of $\vec{V_a}^{(p)}$ on the tangent plane, $\vec{x_{k0}}^{(p)}$ and $\beta^{(p)}$ are obtained. Using the 3D lifting line model, for the kite at α_g, $\gamma^{(p)}$, and $\beta^{(p)}$, with respect to $\vec{x_{k0}}^{(p)}$ and $\vec{z_{k0}}$, with the kinematic defined by $\vec{V_K}^{(p)}$ and $\vec{\Omega}^{(p)}$, in the wind $\vec{V_{RW}}$, one obtain the aerodynamic resultant $\vec{F_a}^{(p)}$ and the updated lift-to-drag ratio $\varepsilon^{(p+1)}$. This force is naturally misaligned with respect to the equivalent tether direction $\vec{z_{k0}}$, while it should be the case according to the zero-mass hypothesis. To partially satisfy this equilibrium condition, the roll angle is firstly updated to $\gamma^{(p+1)}$ in order to get $\vec{F_a}^{(p)}$ in the $(K,\vec{x_{k0}}^{(p)},\vec{z_{k0}})$ plane. This has the effect of getting the apparent wind velocity out of the symmetry plane of the kite $(K,\vec{x_b},\vec{z_b})$. To recover this condition,

the yaw angle is secondly updated to $\beta^{(p+1)}$. The whole process is then iterated until convergence of ε, γ, β, according to some small numerical tolerance.

It is found that this algorithm converges rapidly, and requires between approximately 5 iterations in the case of trajectories of big relative radius R/L_T (leading to small roll angles), and 20 iterations for small relative radius cases (leading to high roll angles). When convergence is reach, it is obtained the expected equilibrium characterized by: the effective lift-to-drag ratio, the aerodynamic resultant effectively aligned with the equivalent tether, the apparent wind effectively parallel to the symmetry plane, and the remaining attitudes angles γ and β.

5.2 Results

Numerous calculations have been carried out in order to evaluate the variations of the lift-to-drag ratio ε, of the aerodynamic force $\vec{F_a}$, and of the angles of yaw β and of roll γ, with respect to the radius of the trajectory R, the tether length L_T or the wind velocity V_{RW}. A fixed angle of incidence α_g of 3° have been chosen for the kite.

(a)

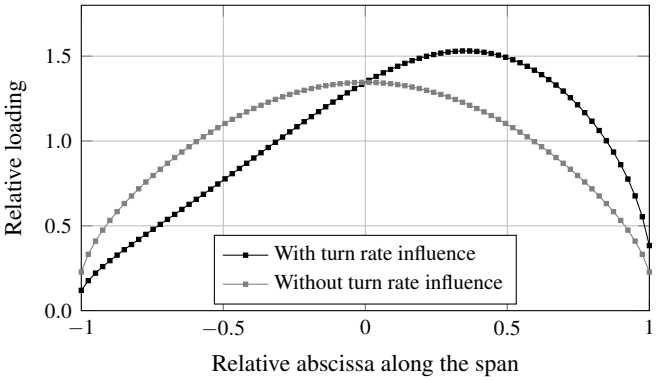

(b)

R	$10m$	ε	10.41
V_{RW}	$5m/s$	C_L	0.52
L_{tether}	$50m$	C_D	0.05
γ	14.6°	V_K	$51m/s$

$$C_L = \frac{L}{0.5\rho V_a^2 S}$$

$$C_D = \frac{D}{0.5\rho V_a^2 S}$$

Figure 10 – (a) Non-dimensional norm of the local aerodynamic resultant along the kite as obtained from the equilibrium procedure, with and without taking into account the turn rate influence. The local norms are divided by the average value of the local norms in the case of the kite in pure translation motion. (b) General flight caracteristics.

Figure 10 shows the influence of the turn rate on the local loading of the kite. The kite follows a trajectory of radius $10m$, with $50m$ of tether length, in a wind velocity of $5m/s$. At convergence, the kite has a velocity of $51m/s$ for a lift-to-drag ratio of 10.41, with the lift estimated from the aerodynamic resultant orthogonal to the apparent wind direction. The black curve represents the relative local loading on the kite as obtained by the iterative equilibrium procedure described section 5.1, while the gray one shows the local loading of the kite with the same apparent wind but assumed to be purely in translation, the turn rate being neglected. The asymmetry of the loading caused by the induced velocities by the turn rate is clearly put in evidence.

(a) (b) (c)

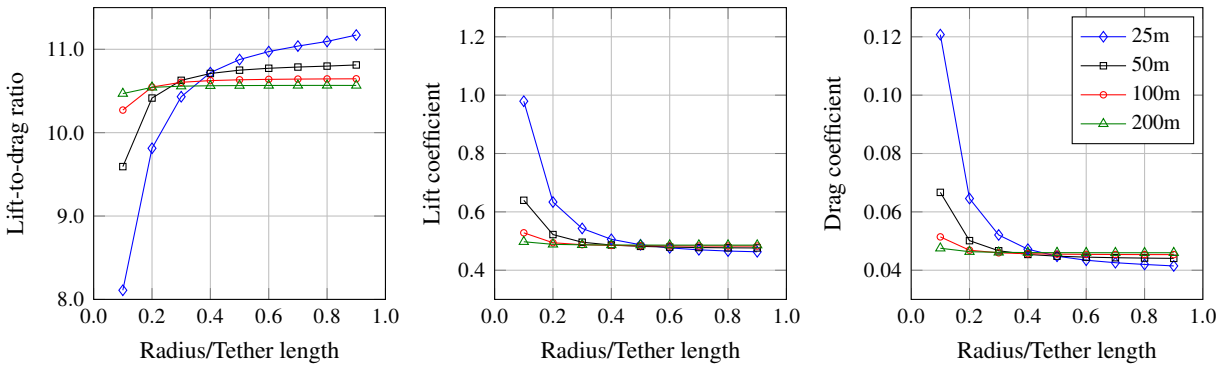

Figure 11 – Evolution of (a) the lift-to-drag ratio, (b) the lift coefficient and (c) the drag coefficient depending on the radius of the trajectory divided by the tether length, and for different lengths of tether from $25m$ to $200m$.

Figure 11 (a) shows the evolution of the lift-to-drag ratio depending on the relative radius, for different lengths of

the tether between $25m$ and $200m$. The lift-to-drag ratio is quasi-constant for longer tether lengths, in contrast it varies substantially for the smaller tether lengths. The same kind of variations can be found for the coefficients of lift and of drag (Figure 11 (b) and (c)). However in this particular case, a diminution of the lift-to-drag ratio corresponds to an increase of the lift coefficient and a faster increase of the drag coefficient.

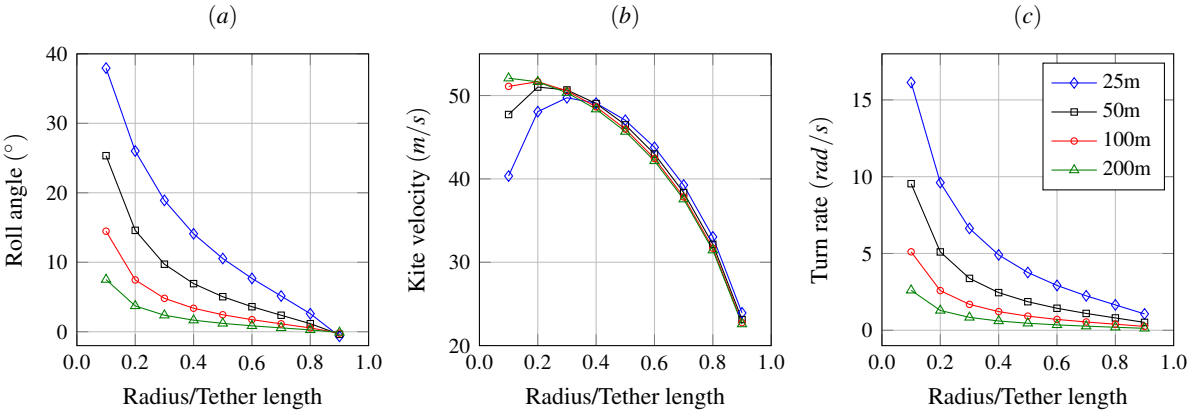

Figure 12 – Evolution of (a) the roll angle, of (b) the kite velocity and of (c) its turn rate depending on the radius of the trajectory divided by the tether length, for different lengths of tether from $25m$ to $200m$.

Figure 12 shows the roll angle, the kite velocity, and the kite turn rate for the same trajectories and the same tether lengths as Figure 11. The results for the roll angles seem to be consistent with intuitive physics of kite: the large angles of roll are obtained in the case of the small radii of trajectory, and vice versa. For high ratio of radius over tether length, the kite velocity is almost the same, while it is more disparate for small relative radius (Figure 12 (b)). Nevertheless, despite the velocity decrease, the turn rate stays high due to the small radius of the trajectory.

5.3 Discussion

A first analysis have been made to study the influence of the real wind velocity V_{RW} by keeping constant all the other parameters. The lift-to-drag ratio, the roll and yaw angle do not vary with respect to V_{RW} while the kite velocity V_K, its turn rate Ω and the apparent wind V_a depends linearly of V_{RW}. This derives logically from the linearity of Equation 1 and Equation 2 (see Section 5.1).

As it can be seen on Figure 11 (a), the lift-to-drag ratio tends to a constant value when the radius of the trajectory increases, the tether length being fixed. The relative radius being fixed, these limit values also reach a constant, when the tether length is increased. This constant value is the lift-to-drag ratio which is obtained neglecting the turn rate influence. Indeed, increasing the radius or the relative radius of the trajectory, one comes closer to cases of pure translation motion.

The lift-to-drag ratio decreases for small radii of the trajectory, while the lift and drag increase (Figure 11), even with a fall of the kite velocity (Figure 12 (b)). This augmentation of the aerodynamic forces is due to the high turn rate of the kite for the small radii of trajectory, which induces high local effective velocities. For the higher radius over tether length ratio, the lift-to-drag ratio is more important for the small tether length. For these cases, the drag force is quasi-identical (between 0.041 and 0.0460) while the lift differs more (between 0.463 and 0.486).

The kite velocity is quite significant. It should be noted that the equivalent tether drag is not taken into account in the iterative equilibrium solution presented section 5.1. The following values are given as an example for the case recalled in Figure 10. The tethers drag has been calculated as Argatov *et al.* [3] by using the formulas from Hoerner [7] with four lines, each of $\delta = 2mm$ of diameter. The new lift-to-drag ratio is 9.13 instead of 10.41, which reduces the kite velocity to $44.7m/s$ instead of $51.0m/s$, after convergence.

The aerodynamic moment is also not taken into account. In fact, it is implicitly assumed that the pitching moment and the rolling moment are equilibrated by differential tensions in the real tethers, respectively front/back and left/right. For the case recalled in Figure 10, the aerodynamic moment about point K is non null. The pseudo-roll component along $\overrightarrow{x_{k0}}$ is found to be the major one, the pseudo-pitch component along $\overrightarrow{y_{k0}}$ is the medium one (5 times smaller), and the pseudo-yaw component along $\overrightarrow{z_{k0}}$ is the minor one (15 times smaller). This last result for the yawing moment is consistent with the assumption made in section 5.1, which states that the yaw angle only results from a self-positioning of the kite.

6 Conclusion

A parametric model of wing has been defined. It allows the construction of kite wings with twist, dihedral and sweep angles. In order to estimate the aerodynamic forces on a kite, a 3D non-linear lifting line method has been developed. This iterative method is adapted to wings non-straight and non-planar and shows a small mesh dependency at low angles of incidence. This method has been validated with 3D RANSE simulations. After a mesh convergence study, the results of the 3D lifting line method show good agreement with the RANSE simulation ones. The difference between the two approaches is of 5% for the lift prediction, 5% for the drag at the lower angles of incidence, up to 20% near stall conditions. The gap for the moment coefficient is almost constant around 12%. This model has then be used for the prediction of the aerodynamic forces on a kite in dynamic flight on a circular trajectory. An iterative equilibrium procedure has been developped, based on zero-mass model assumptions, but taking into account the turn rate of the kite. The results show the non-negligible influence of the turn rate of the kite on its performances and the induced asymmetry of the local loading of the lite.

However this method, by lining up aerodynamic resultant and kite equivalent tether, neglect the kite moment equilibrium, assumed to result from differential tensions in the real tethers. The next step will be to take this moment equilibrium into account and to balance the kite on any arbitrary trajectory, and not only a circular one. Furthermore, experimental measurements on a kite on eight shaped trajectories have been conducted elsewhere in the research program related to the beyond the sea® project. They have allowed getting the wind velocity, the tensions in the tethers, the position of the kite and its velocity depending on variations of the tethers length. The post-processing of these measurements will provide validation data for the model and its evolutions.

Acknowledgment:

The authors would like to thank the French Environment & Energy Management Agency (ADEME).

References

[1] I.H. Abbott and A.E. von Doenhoff. *Theory of wing sections*. Dover, 1959.

[2] J.D. Anderson. *Fundamentals of aerodynamics*. McGrawHill, 5th edition, 2011.

[3] I. Argatov, P. Rautakorpi, and R. Sivennoinen. Apparent wind load effects on the tether of a kite power generator. *Journal of Wind Engineering and Industrial Aerodynamics*, 99:1079–1088, 2011.

[4] G. Dadd, D.A. Hudson, and R.A. Shenoi. Determination of kite forces using three-dimensionnal flight trajectories for ship propulsion. *Renewable Energy*, 36(10):2667–2678, 2011.

[5] M. Gaunaa, P. Carqueija, P.-E. Réthoré, and N. Sorensen. A computationally efficient method for determining the aerodynamic perfomace of kites for wind energy applications. 2011.

[6] K. Graf, A.V. Hoeve, and S. Watin. Comparison of full 3d-rans simulations with 2d-rans/lifting line method calculations for the flow analysis of rigid wings for high performance multihulls. *Ocean Engineering*, 90:49–61, November 2014.

[7] S. F. Hoerner. *Fluid-dynamic drag*. Hoerner Fluid Dynamics, 1965.

[8] J. Katz and A. Plotkin. *Low speed aerodynamics*. Cambridge University Press, 2001.

[9] R. Leloup. *Model approach and numerical tool development for kite performance assesment and mechanical design; application to vessels auxiliary propulsion*. PhD thesis, ENSTA Bretagne/UBO, 2014.

[10] R. Leloup, Roncin K., G. Bles, J. Leroux, C. Jochum, and Y. Parlier. Estimation of the lift-to-drag ratio using the lifting line method: application to a leading edge inflatable kite. *Airborne Wind Energy*, 2013.